Biol Cybern (2008) 99:63–78
DOI 10.1007/s00422-008-0238-9

ORIGINAL PAPER

Biological
Cybernetics

Symmetries, non-Euclidean metrics, and patterns in a Swift–Hohenberg model of the visual cortex

N. Michael Mayer · Matthew Browne ·
J. Michael Herrmann · Minoru Asada

Received: 18 October 2006 / Accepted: 27 April 2008 / Published online: 21 June 2008

Abstract The aim of this work is to investigate the effect of the shift-twist symmetry on pattern formation processes in the visual cortex. First, we describe a generic set of Riemannian metrics of the feature space of orientation preference that obeys properties of the shift-twist, translation, and reflection symmetries. Second, these metrics are embedded in a modified Swift–Hohenberg model. As a result we get a pattern formation process that resembles the pattern formation process in the visual cortex. We focus on the final stable patterns that are regular and periodic. In a third step we analyze the influences on pattern formation using weakly nonlinear theory and mode analysis. We compare the results of the present approach with earlier models.

Keywords Orientation maps in visual cortex · Pattern formation process · Shift-twist symmetry

N. Michael Mayer (✉) · M. Asada
JST ERATO Asada Project, FRC-I, Graduate School
of Engineering, Osaka University, 2-1 Yamada-oka, Suita,
Osaka 565-0871, Japan
e-mail: michael@jeap.org

M. Browne
CSIRO, PO Box 120, Cleveland, QLD 4163, Australia

J. M. Herrmann
University of Edinburgh, Institute for Perception, Action and
Behaviour Informatics Forum, 10 Crichton Street,
Edinburgh EH8 9AB, UK

J. M. Herrmann
Bernstein Center for Computational Neuroscience Göttingen,
Bunsenstr. 10, 37073 Goettingen, Germany

Variables

$G(x, y, \mathbf{v})$	Elongated Gaussian distribution
$\hat{R}(\Phi), \hat{T}(\Psi)$	2×2 rotation matrices
d_s^2	Distance between stimuli, between receptive fields and stimuli
x, y, z_1, z_2	Real-valued features
$\mathbf{x}, \mathbf{z}$	Complex features
$\mathbf{v}$	Feature vector
$\mathcal{V}$	Feature space – manifold
$\hat{g}, g_{ij}$	Metric tensor
a, b, c, h	Parameter functions of the metric tensor
β, γ, μ, ν	Parameter functions in complex coordinates

1 Introduction

Spike rates of neurons in the visual cortex depend on the type of visual stimulation. The specific properties of each neuron are typically investigated by exposing the subject to a stimulus with a certain set of features, e.g., orientation, position in the visual field, and others. The activity of this neuron is then recorded with respect to the presented stimulus. Optical imaging experiments show not only that single neurons show a preference for certain features, but also that each point of the cortex surface is activated by a set of specific preferred stimulus features. Neurons with similar stimulus preferences tend to be grouped together in one small area on the cortical surface. These preferences typically change continuously as a function of the position on the cortex surface and form a structure which shows a two-dimensional pattern (map) of a certain wavelength. This is represented by a map from the cortex to the feature space, called the feature map. The image of this map roughly covers the whole feature space, i.e., all possible combinations of features (Swindale et al. 2000).

Feature maps of the cortex are interesting since experiments have shown their dependence on stimuli (e.g., Löwel 1998). Thus, models of feature maps are often seen as a result of a stimulus-driven self-organizing process (see, however, Ernst et al. (2001) for an example of a different type of model). In particular, computational models of feature maps in the visual cortex have a long history (Malsburg 1973; Swindale 1996). Most models assume that the visual cortex undergoes an optimization process of two competing optimization criteria: (1) optimal folding of the map into the complete space of preferred stimuli (called the short stimulus space herein) and (2) neighborhood preservation. Both criteria, optimal coverage and neighborhood preservation, are dependent on assumptions on the underlying metrics of the stimulus space, and its features, respectively. One type of mapping algorithm represents the relevant features internally as scalar values rather than as activity distributions. These low-dimensional or feature models give useful qualitative insights into corresponding adaptation processes. Simulations of feature models require relatively little numerical effort. In addition, theoretical results are available for these kinds of maps (Ritter et al. 1992).

Alternative high-dimensional approaches internally represent the activity of afferent geniculate fibers as a distribution over a two-dimensional array of pixels. Thus, features such as orientation and retinal position are coded implicitly as properties of activation patterns and can be extracted by a subsequent analysis of high-dimensional receptive field data after the learning process.

Focusing on early and intermediate states of development, maps from low-dimensional models do not differ essentially from feature maps that are extracted from their high-dimensional counterpart. In later stages of the development the pattern usually converges to a stable fixed point, which is a periodic pattern.

One important goal is to find quantifiable criteria of equivalences between models of the visual cortex and those maps found in the visual cortex. Several investigations (Wolf 2005; Wolf and Geisel 1998, 2003) have drawn attention to the occurrence of annihilation processes of pinwheels and the density of pinwheels in orientation maps. Pinwheels are points in the orientation map that neighbor all orientations. They are prominent and easily detectable from the layout of any orientation map. In particular, the density of pinwheels on the maps of orientation preferences after long learning processes has been investigated in the last cited works. Based on the analysis of feature models it was shown therein that, for some classes of model, no stable nonvanishing pinwheel density exists if the lateral interaction between the neurons is restricted to nearest-neighbor interactions. However, many types of stable patterns that contained pinwheels could be constructed by adding nonlocal nonlinear interaction kernels to the dynamic equation. The conclusion that was drawn from these works was that the lateral long-range connections in the cortex are responsible for the appearance of nonvanishing pinwheels in adult animals. In this work only local interactions are considered and we assume a four-dimensional manifold of stimulus preferences (henceforth called the stimulus manifold herein), in which there are two dimensions for the position of the stimulus preferences in the visual space and two dimensions for orientation and orientation preference.

The main aim of this work is to understand from a more analytical point of view earlier numerical results using the elastic neural net approach (Mayer et al. 2002) in which it was shown that, depending on the metric applied, two types of stable patterns were observed. More precisely we investigated a coupling between the position shift and the orientation preference that affects the metrics. The coupling and the remaining symmetry constraints have been recently introduced as a shift-twist symmetry (Thomas and Cowan 2003).

In investigations of natural image statistics (Kaschube et al. 2001) it has been found that spatial correlations in all kinds of everyday environments (forest, parks, inner city views, etc.) along co-linear contour segments are larger than across those segments. Under the assumption that the formation of both receptive fields and orientation maps are affected, one would expect some kind of coupling term in the feature metrics, reflecting these statistical properties. That the natural image statistics are indeed affected by the shape of receptive fields is strongly suggested by a model investigating the receptive field formation at different stages of early postnatal retinal development (Mayer et al. 2001). In addition, several experiments have shown that feature maps, including orientation maps, are affected by experience (see, e.g., Sengpiel et al. 1999).

In Sect. 2 and Appendix C we justify our approach, and in Sect. 3 we outline how an appropriate metric can be derived from very basic symmetry constraints.

In Sect. 5 we introduce the Swift–Hohenberg approach and describe how we modify this approach to embed our metrics. The Swift–Hohenberg (SH) approach has been used in Wolf's work (Wolf 2005; Wolf and Geisel 2003, 1998) and has been proved to be analytically easier to handle than other mapping approaches such as self-organizing maps and elastic nets.

In Sect. 6 we report results from numerical experiments, using the SH approach for different metrics, and show that the evolution and the final maps depend on the development. The results can be explained by Fourier transforming and then deriving the equations of the components (modes), which is done in Sect. 7. Based on the analytical mode equations we investigate for what various types of metrics what patterns are stable. In Sect. 8 we describe the numerically derived phase-space structure for the variant metrics. We close with an outline of our derived periodic patterns and discuss reasons why those patterns do not normally appear in animals.

2 Advantages of Riemannian feature metrics

In this section we give a simple heuristic example in which the diagonal Euclidean distance measure of feature coordinates is not appropriate to describe distance relations of a very basic high-dimensional model of orientation preference.

In our high-dimensional model, the input space is described as a square array of input fibers. The stimulus set is chosen as a set of 2D Gaussian distributions ("blobs") in which one direction is elongated (cf. Fig. 1). We assume a stimulus manifold $\mathcal{V}$ in this high-dimensional space with the parameters (features) $\mathbf{v} = \{\langle x\rangle, \langle y\rangle, \Phi, S\}$. A 2D Gaussian,

$$G(x, y, \mathbf{v}) = \exp\left(-\left\| \begin{pmatrix} s_a(S) & 0 \\ 0 & s_b(S) \end{pmatrix} \cdot \hat{R}(\Phi) \cdot \begin{pmatrix} x - \langle x\rangle \\ y - \langle y\rangle \end{pmatrix} \right\|^2\right), \quad (1)$$

with $\hat{R}(\Phi)$ being a 2 × 2 rotation matrix of the angle Φ, and s_a and s_b functions of the orientation strength, can be defined as the activity pattern. In this way the orientation strength S can be expressed as the differences of the variances of the Gaussian across and along the preferred orientation. The distance d_s^2 between two stimuli G_1 and G_2 can be defined as

$$d_s^2 = \int \mathrm{d}x\mathrm{d}y\, (G_1(x, y, \mathbf{v}) - G_2(x, y, \mathbf{v} + \Delta\mathbf{v}))^2 . \quad (2)$$

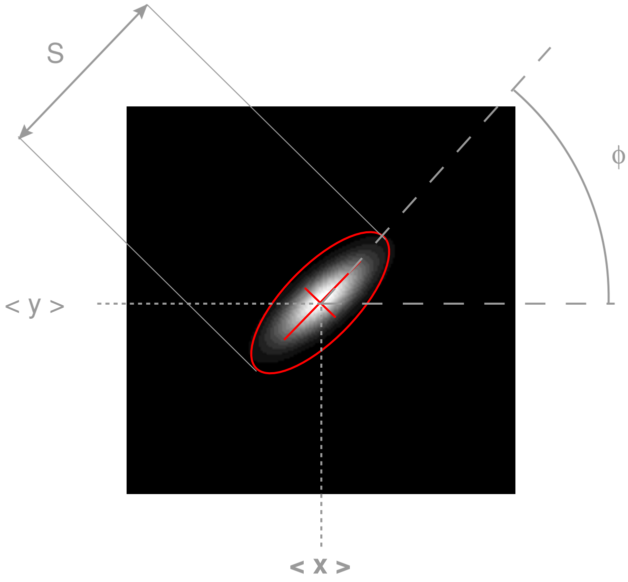

Fig. 1 Model stimulus: A simplified stimulus in the proposed high-dimensional model is a two-dimensional Gaussian distribution elongated in one direction. The value of the elongation S indicates the strength of the orientation preference, the angle Φ of the direction of the elongation gives the preferred orientation, and averages of the distribution give the positions x and y in the visual field

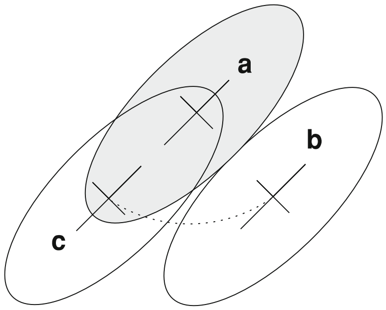

Fig. 2 Three high-dimensional stimuli with the same orientation: One simplified stimulus is translated parallel to and the other perpendicular to the orientation of the third stimulus **a**. Though both input profiles have the same center distance in retinal coordinates, the overlap for **b** is smaller than that for **c**

In the following we assume $\|\Delta\mathbf{v}\|$ small and thus $d_s^2 \approx \Delta\mathbf{v}^T\, \hat{g}\, \Delta\mathbf{v}$, where $\hat{g}$ represents a 4 × 4 metric tensor. Every entry g_{ij} of this tensor is a function of $\mathbf{v}$.

In this section we restrict ourselves to a heuristic analysis. For this purpose consider Fig. 2. We see three oval shapes representing three stimuli **a**, **b**, **c**. In a typical feature-type approach a distance measure consisting of a diagonal metric tensor is assumed, i.e., the distance between the stimuli is $d_s^2 = (\langle x_1\rangle - \langle x_2\rangle)^2 + (\langle y_1\rangle - \langle y_2\rangle)^2 + d(\Phi_1, \Phi_2, S_1, S_2)$, where $d(\Phi_1, \Phi_2, S_1, S_2)$ is some—for the moment unspecified—distance between the orientations of two stimuli. In Fig. 2 the orientation preference and orientation strength are the same for all three stimuli, thus $d(\Phi_1, \Phi_2, S_1, S_2)$ vanishes; $d_s^2 = (\langle x_1\rangle - \langle x_2\rangle)^2 + (\langle y_1\rangle - \langle y_2\rangle)^2$ remains. Since the center of **b** has the same distance to **a** as **c** the distance from this ds^2 (i.e., resulting from a diagonal tensor) would be the same in both cases.

However, the figure shows a larger overlap between **a** and **c** than between **a** and **b**. Since a larger overlap indicates a smaller distance, the distance between **a** and **b** should be smaller than the distance between **a** and **c**. Thus, the overlap and the distance depend on the direction of the displacement and the orientation. In the following section a method is described to derive such a Riemannian metric that accounts for this situation. At the same time the metric should be invariant under symmetry operations that are assumed to apply at least to the above described set of stimulus preferences, and to some degree also to the situation in the visual cortex.

3 A feature metric based on symmetry considerations

In this section we discuss properties of the stimulus space, which we assume to be a Riemannian manifold. We formulate symmetry transformations under which the Riemannian metric remains invariant. By formulating those symmetries the mathematical form of the metric obeying those invariants can be relatively easily narrowed down to a convenient general shape.

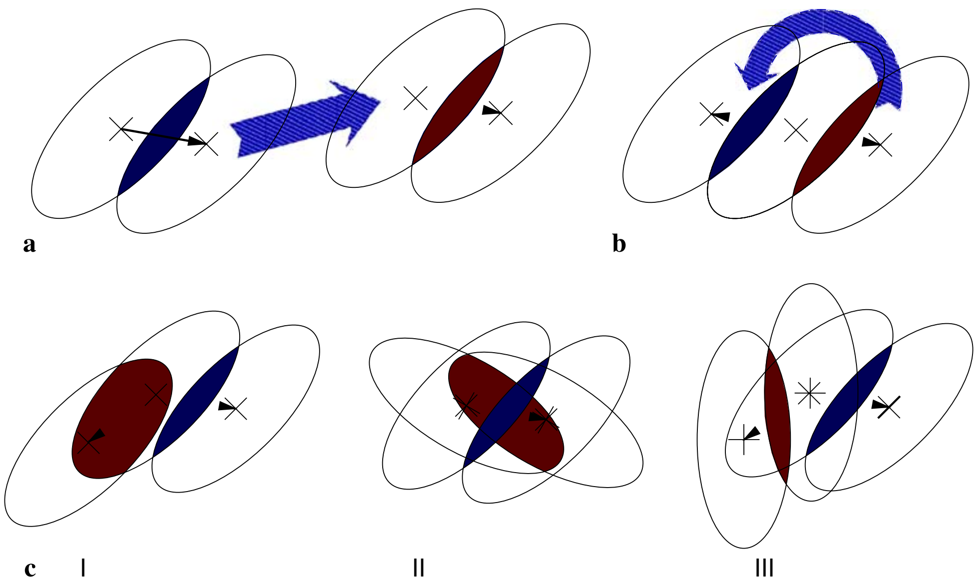

Fig. 3 **Symmetries:** the overlap of the high-dimensional approach is invariant under translation (**a**), inversion of position difference (**b**), and combined rotation of position difference and orientation preference (**c**, case III). However, the overlap changes if either the position difference is rotated independently (**c**, case I) or the orientation preference is rotated independently (**c**, case II)

In the following we use for the feature space $\mathcal{V}$ the coordinates[1]

$$\mathbf{v} = [x, y, z_1 = S\ \sin(2\Phi), z_2 = S\ \cos(2\Phi)], \tag{3}$$

where x and y indicate the the position of the preferred stimulus in the visual field, Φ the orientation of the preferred stimulus, and $\|z\| = S$ the orientation strength. This parametrization gives us an appropriate topological mapping to describe the complete stimulus manifold by one set of parameters. In addition, where it is more convenient, the complex notation of coordinates is used

$$\mathbf{x} = x + \mathrm{i}y, \tag{4}$$

$$\mathbf{z} = z_1 + \mathrm{i}z_2, \tag{5}$$

where i represents an imaginary unit. In the remaining part of the section we investigate the metric tensor

$$d_s^2 = \Delta\mathbf{v}^T \hat{g}(\mathbf{v})\Delta\mathbf{v}, \tag{6}$$

where $\hat{g}$ represents a symmetric 4×4 matrix of scalar entries $g_{ij} = g_{ji}$, of which each can be at this stage an arbitrary function of $\mathbf{v}$.

In the following, symmetric operations are outlined for which we assume the feature metric to be invariant:

S1 The distance between two high-dimensional stimuli is invariant under shifts of the position in the visual space (Fig. 3a). As a consequence, the tensor should be invariant under translations of x and y. Therefore, none of the g_{ij} should be functions of x and y. In the visual cortex this assumption is almost true in the part of the visual cortex that corresponds to foveal vision.

S2 The simplified stimulus shows a reflection symmetry along and across the preferred orientation. This has several consequences. For the moment we use that the distance between two high-dimensional stimuli does not change if the position shift (dx, dy) is inverted (Fig. 3b). This means that the terms g_{13}, g_{14}, g_{23}, g_{24}, and their corresponding counterparts[2] become 0.

S3 The distance between two high-dimensional stimuli does not change if both the orientation and the position difference are rotated (Fig. 3c) (case III). Please note that the metric is not necessarily invariant under rotation of the position difference (case I) and it is not necessarily invariant under the rotation of both orientation preferences (case II). Thus, the feature metrics should be invariant under the combined rotation of position x, y and orientation preference z_1, z_2. This has two consequences. First, the g_{ij} can only be functions of $\|z\|$. Second, the metrics can only be made of the sum of the following square expressions:

$$d_s^2 = a(\|z\|)\,(dx^2 + dy^2) + b(\|z\|)(dz_1^2 + dz_2^2) \\ +C_{xz} + C_{zz}. \tag{7}$$

The two coupling terms C_{xz} and C_{zz} are restricted[3] to the form

$$C_{xz} = c(\|z\|)\begin{pmatrix} z_1 \\ z_2 \end{pmatrix}^T \mathbf{T}(\psi)\begin{pmatrix} dx^2 - dy^2 \\ 2dxdy \end{pmatrix} \tag{8}$$

$$C_{zz} = h(\|z\|)\left(\begin{pmatrix} z_1 \\ z_2 \end{pmatrix}^T \begin{pmatrix} dz_1 \\ dz_2 \end{pmatrix}\right)^2 \tag{9}$$

---

[1] From here on, x and y are used instead of $\langle x\rangle$ and $\langle y\rangle$, respectively.

[2] Since $\hat{g}$ is a symmetrical matrix also g_{31}, g_{41}, g_{32}, and $g_{42} = 0$.

[3] A more detailed discussion of the coupling terms and the effects of S3 can be found in Appendix B.

$\mathbf{T}(\psi)$ is a two-dimensional matrix of the rotation by an angle ψ. In simple words ψ indicates the angle at which the direction of the position displacement $[dx, dy]$ is coupled to the orientation preference. For the analysis of the coupling and the derivation of the characteristics of Ψ see Appendix B.

We can further simplify the metrics by regauging the orientation preference. Thus, z_1 and z_2 are redefined to

$$\begin{pmatrix} z_{1,\text{new}} \\ z_{2,\text{new}} \end{pmatrix} = \mathbf{T}(\psi) \begin{pmatrix} z_{1,\text{old}} \\ z_{2,\text{old}} \end{pmatrix}. \tag{10}$$

A little consideration shows that this encoding of the orientation preference means that the orientation vectors $(1, 0)$ and $(-1, 0)$ represent stimuli where the symmetry axes from the **S2** symmetry coincide with the x and y axes, respectively. In this way the matrix T can be diagonalized to the identity matrix and we get for g_{ij}

$$\hat{g} = \begin{pmatrix} a + cz_1 & cz_2 & & \\ cz_2 & a - cz_1 & & \\ & & b + hz_1z_1 & h\ z_1z_2 \\ & & hz_1z_2 & b + h\ z_2z_2 \end{pmatrix}. \tag{11}$$

3.1 α-Metric

In Appendix C it is shown how any metric that complies with Eq. (11) can be mapped to a set of equivalence classes by redefining the orientation strength $\|z\|$ and eliminating h.

For any equivalence class we can approximate the elements of this class to the metric $\hat{g}_\alpha$ as (See Appendix A for the parameter functions in the case of the metric of the Gaussians outlined in Sect. 2.)

$$\hat{g}_\alpha = \begin{pmatrix} 1 + \alpha z_1 & \alpha z_2 & & \\ \alpha z_2 & 1 - \alpha z_1 & & \\ & & 1 & \\ & & & 1 \end{pmatrix} \tag{12}$$

for small values of $\|z\|$. As outlined in the Appendix (Appendices A–C) the present form of the d_s^2 and the α can be seen as a mathematically pure form of the situation depicted in Fig. 2.

Here, the value of α is a constant that represents a coupling between orientation and position. We use α in the following as a parameter in order to test the relevance of the coupling for the evolution of different patterns. It represents the difference of the distance along and across the preferred orientation and obeys at the same time the above mentioned symmetry constraints. If α is zero the metric is a usual feature metric and the results of other approaches can be compared. Thus, except for $\alpha = 0$, the metrics contain a coupling between position and orientation preference and are neither diagonal nor Euclidean. For several reasons it is useful to use complex coordinates $\mathbf{z} = z_1 + \mathrm{i}z_2$ and $\mathbf{x} = x + \mathrm{i}y$. In terms of these the metric can be expressed as

$$d_s^2 = \mathrm{Re}(\mathrm{d}\mathbf{z}\,\mathrm{d}\bar{\mathbf{z}} + \mathrm{d}\mathbf{x}\,\mathrm{d}\bar{\mathbf{x}} + \alpha\bar{\mathbf{z}}\,\mathrm{d}\mathbf{x}^2), \tag{13}$$

where $\mathrm{Re}(x)$ denotes the real part of $x \in \mathbb{C}$, $\mathrm{d}\mathbf{z}$ and $\mathrm{d}\mathbf{x}$ represent the displacement of two stimuli with infinitesimal distances. $\mathrm{d}\bar{\mathbf{z}}$, $\mathrm{d}\bar{\mathbf{x}}$, $\bar{\mathbf{z}}$, and $\bar{\mathbf{x}}$ represent the complex conjugate of $\mathrm{d}\mathbf{z}$, $\mathrm{d}\mathbf{x}$, $\mathbf{z}$, and $\mathbf{x}$, respectively.

4 Relation to a metric between V1 complex cell receptive fields

Reverse correlation methods revealed that the receptive fields of V1 receptive fields of simple cells are Gabor filters (Jones and Palmer 1987). Simple cell receptive fields resemble Gabor filters. That means that they do not obey the reflection symmetry across the preferred orientation (**S2**). In addition, it is difficult to include all features of simple cell receptive fields in a four-dimensional feature space. However, other considerations (Mayer et al. 1998) also show that it is very difficult to construct a high-dimensional self-organizing map model basing on simple cell receptive fields. Herein pieces of natural images are used as a stimulus. In effect, Gabor filters result from this input. However, some basic problems arise from the representation of the spatial phase upon the map. As a consequence, stable maps with a retinotopic structure seem rather difficult if not impossible to create, for reasons that can be seen from very basic, again metric, considerations. As an alternative, herein maps of adaptive subspace self-organizing maps (ASSOMs) are suggested as a more appropriate model for V1. In an ASSOM each node represents a superposition of two or more adaptive base vectors. For each stimulus the closest representative upon the map is defined by the minimum over the superposition of these two basis vectors. As a consequence, each node behaves in a way that resembles cortical complex cell receptive fields. The spatial phases of the Gabor filters are not represented as a feature upon the map surface, which is probably also true for the real V1 (Pollen and Ronner 1981; Liu et al. 1991; Freeman et al. 1997). It is therefore useful to investigate the relation with the metric that arises from complex receptive field properties. Thus it is useful to consider the following metric, which can be seen as derived from these ideas. Thus a complex cell receptive field of the feature vector $\mathbf{v} = [x, y, S, \phi]$ can be represented as a superposition of the two base vectors Γ_s (reflection symmetric) and Γ_a (antisymmetric):

$$\Gamma_s(x, y, \mathbf{v}) = \exp\left(- \left\| \begin{pmatrix} x - \langle x \rangle \\ y - \langle y \rangle \end{pmatrix} \right\|^2 / (2\sigma^2) \right) \\ \times \cos\left([x - \langle x \rangle, y - \langle y \rangle]\, \hat{R}(\phi) \begin{bmatrix} S \\ 0 \end{bmatrix} \right), \tag{14}$$

$$\Gamma_a(x,y,\mathbf{v}) = \exp\left(-\left\|\begin{pmatrix} x-\langle x\rangle \\ y-\langle y\rangle \end{pmatrix}\right\|^2 /(2\sigma^2)\right) \times \sin\left([x-\langle x\rangle, y-\langle y\rangle]\,\hat{R}(\phi)\begin{bmatrix} S \\ 0 \end{bmatrix}\right). \tag{15}$$

In this way the response λ of a neuron to a high-dimensional receptive field $\Sigma(x, y)$ can be modeled as

$$\lambda = \min_{\psi} \int \|\Sigma(x,y) - \Gamma_r(\psi,x,y,\mathbf{v})\|^2 \,\mathrm{d}x\mathrm{d}y, \tag{16}$$

where

$$\Gamma_r(\psi,x,y,\mathbf{v}) = \cos(\psi)\Gamma_a(x,y,\mathbf{v}) + \sin(\psi)\Gamma_s(x,y,\mathbf{v}). \tag{17}$$

A corresponding metric can be defined as

$$d_s^2(\mathbf{v},\Delta\mathbf{v}) = \min_{\psi_1,\psi_2} \int \|\Gamma_r(\psi_1,x,y,\mathbf{v}+\Delta\mathbf{v}/2) - \Gamma_r(\psi_2,x,y,\mathbf{v}+\Delta\mathbf{v}/2)\|^2 \,\mathrm{d}x\mathrm{d}y. \tag{18}$$

Different from the metrics that can be derived from simple cell receptive fields this type of metric complies with the symmetry S2.

5 Models

In the context of the models discussed in this work the cortex is assumed to be a two-dimensional plane in which points are indexed as $\mathbf{r} \in \mathcal{R}^2$. As outlined in the introduction, we assume a model of topographical representations of stimulus features. More precisely, we assume that each point of the cortex surface contains neurons that have receptive field properties within a subset $\mathcal{W}_\mathbf{r} \subset \mathcal{V}$ of the feature space that is small enough that it can be described sufficiently accurate by one average feature vector $\langle \mathcal{W}_\mathbf{r} \rangle = \mathbf{w}_\mathbf{r}$.

In the following the metric as derived in Eq. (12) is used to find a map $\mathbf{w}_\mathbf{r}$ that is optimal with respect to the two optimization criteria mentioned in the introduction: (1) neighboring neurons represent as near as possible points in the feature space and (2) one cortical area as a whole is optimized to fill the complete feature space as densely as possible. Criterion 2 can also be formulated as follows: for each point in feature space the nearest representation upon the cortical surface should be as close as possible. Note that both criteria depend on what is assumed to be the appropriate distance measure.

As outlined in the introduction, many models of maps of the visual cortex either implicitly or explicitly optimize their maps to these two criteria. The aim of our numerical experiments is to find how the map formation process is affected by applying variant metrics to these models and what stable patterns emerge after a sufficiently long adaptation process.

In the following we introduce the feature elastic net (ELN) algorithm, which has been used in previous models, then for comparison a high-dimensional self-organizing map (HSOM), and finally a modified Swift–Hohenberg approach.

5.1 Feature ELN

We follow the approach as described in Mayer et al. (2002), which is a modification of the initial approach described by Durbin and Willshaw (1987). The metric has been built into a modified two-dimensional elastic net approach, where the energy function consists of

$$E_{\mathrm{eln},1} = -A\left\langle \log\left(\sum_{\mathbf{r}\in\mathcal{N}} \exp\left(-\frac{d^2(\mathbf{v},\mathbf{w_r})}{2\sigma^2}\right)\right)\right\rangle_{\mathbf{v}\in\mathcal{V}} \tag{19}$$

and

$$E_{\mathrm{eln},2} = B\sum_{\mathbf{i}\in\mathcal{N}}\sum_{\|\mathbf{i}-\mathbf{j}\|=1} d^2\left(\mathbf{w_i},\mathbf{w_{r}}_j\right). \tag{20}$$

The model was initialized with $\mathbf{w_r} = \{n_1, n_2, \rho r_1, \rho r_2\}$, where ρ is a constant proportionality factor that defines the relation between the position of the receptive field in the cortex and the position in retinal coordinates, and n_1 and n_2 represent a small noise component added to the orientation preference of zero. The cost function $E_{\mathrm{eln}} = E_{\mathrm{eln},1} + E_{\mathrm{eln},2}$ was optimized using simple gradient descent. $\mathcal{N}$ represents a periodic two-dimensional grid and $\mathcal{V}$ the stimulus space. The parameters A and B control the stiffness of the map and were chosen to keep the dynamics in a state that showed only weak orientation preferences (Mayer et al. 2002). Looking more closely at each of the components of $E_{\mathrm{eln},1}$ and $E_{\mathrm{eln},2}$ one can see that $E_{\mathrm{eln},1}$ is the component that explicitly optimizes the entropy of the map points within the stimulus space, that is, lets the map cover the stimulus space as well as possible, whereas the second component minimizes the distance of nearest neighbors in the stimulus space. Thus, in the case of the elastic net algorithm, both competing optimization criteria mentioned in the introduction appear explicitly as summands of the energy function. The case of the plane metric is well investigated and the points of phase transitions are known; examples are shown in Fig. 4.

5.2 High-dimensional self-organizing map

The self-organizing map algorithm (Kohonen 2001) has often been used to model pattern formation processes. Different from the ELN, no general cost function exists and the algorithm is defined by the dynamics

$$\mathbf{W_r} = \epsilon(\mathbf{V} - \mathbf{W_r})\exp\left(-\frac{\|r-r^*\|^2}{2\sigma_k^2}\right), \tag{21}$$

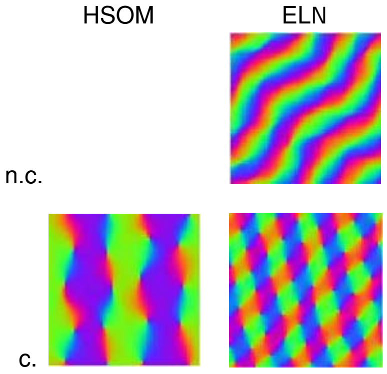

Fig. 4 **Earlier models with C_{xz} coupling :** Depicted are three model types: a high-dimensional self-organizing map (*HSOM, left*), elastic net (feature approach) (*ELN, right*). *Above*: uncoupled ($\alpha = 0.0$), *below* coupled (ELN: $\alpha = 0.3$). Since the HSOM is high dimensional, a version without coupling does not exist. For simulation details see Sects. 5.1 and 5.2

where

$$r^* = \text{argmin}_r \, (\mathbf{V} - \mathbf{W_r})^2 \tag{22}$$

and σ_k is the neighborhood length of the net, which controls the stiffness of the Kohonen net in a similar way to the parameter B in the ELN approach above. In the HSOM the folding in the stimulus manifold is achieved by the iterative adaptation of the respective winner neuron r^* towards the stimulus.

Figure 4 shows an example of an HSOM orientation map with 64 × 64 neurons; the input space of each neuron was 24 × 24 pixels. The approach had periodic boundary conditions. The neurons were initialized retinotopically with round Gaussian blobs. Stimulation was done by elongated 2D Gaussian blobs with standard deviations of 7.46 and 2.15. The neighborhood length was 5.0. The values have been chosen to be near to the nonselective phase (see Riesenhuber et al. 1998 for details).

5.3 Swift–Hohenberg approach

We start the discussion from the complex Swift–Hohenberg equation (SHE) (Wolf and Geisel 2003; Cross et al. 1993), that is,

$$\partial_t \mathbf{z} = \epsilon \mathbf{z} - (\Delta + k_{\text{crit}}^2)^2 \mathbf{z} - \|\mathbf{z}\|^2 \mathbf{z}. \tag{23}$$

The linearized dynamic equations around $\mathbf{z} = 0$ are

$$\partial_t \mathbf{z} = \epsilon \mathbf{z} - (\Delta + k_{\text{crit}}^2)^2 \mathbf{z}. \tag{24}$$

Fourier transformation of this linear equation results in

$$\partial_t \tilde{\mathbf{z}} = \epsilon \tilde{\mathbf{z}} - (-\|\mathbf{k}\|^2 + k_{\text{crit}}^2)^2 \tilde{\mathbf{z}}, \tag{25}$$

where $\tilde{\mathbf{z}}(\mathbf{k})$ is the Fourier transform of $\mathbf{z}(\mathbf{r})$. If ϵ is smaller than 0, all $\tilde{\mathbf{z}}(\mathbf{k})$ have dynamics with negative eigenvalues and thus the state $\tilde{\mathbf{z}}(\mathbf{k}) = 0$ is stable. For a small positive ϵ, only $\tilde{\mathbf{z}}(\mathbf{k})$ with positive feedback, i.e., $\tilde{\mathbf{z}}(\mathbf{k})$ with $\|\mathbf{k}\|$ of around k_{crit}, can proliferate. The relation to the two models above can be seen by writing Eq. (23) as

$$\partial_t \mathbf{z} = \epsilon \mathbf{z} - \Delta^2 \mathbf{z} - k_{\text{crit}}^4 \mathbf{z} - \|\mathbf{z}\|^2 \mathbf{z} - 2k_{\text{crit}}^2 \Delta \mathbf{z}. \tag{26}$$

Only the last term on the right-hand side relates to the neighborhood preservation force, whereas the other terms of the equation are equivalent to the first-order folding of the map into the stimulus space.

In the following, we consider how the part of the equation that relates to the neighborhood preservation can be modified to comply with the α metric.

For the sake of simplicity the other terms that relate to the folding of the map into the feature space remain as in the previous case.

We introduce the cost function E_{sh} for which the gradient descent $\partial_t \mathbf{w} = -\delta_{\mathbf{w}} E_{\text{sh}}$ results in the dynamics of the SHE. We write the energy in four terms

$$E_{\text{sh}} = \sum_{i=1}^{4} E_{\text{sh},i}, \tag{27}$$

which are

$$E_{\text{sh},1} = -\frac{\epsilon - k_{\text{crit}}^4}{2} \int z_1^2 + z_2^2 + \xi_1^2 + \xi_2^2 \mathrm{d}\mathbf{r}, \tag{28}$$

$$E_{\text{sh},2} = +k_{\text{crit}}^2 \int \left(\frac{\partial \mathbf{w}}{\partial r_1} \, \hat{g}_\alpha \, \frac{\partial \mathbf{w}}{\partial r_1}^T + \frac{\partial \mathbf{w}}{\partial r_2} \, \hat{g}_\alpha \, \frac{\partial \mathbf{w}}{\partial r_2}^T \right) \mathrm{d}\mathbf{r}, \tag{29}$$

$$E_{\text{sh},3} = +\frac{1}{2} \int \|\Delta \mathbf{w}\|^2 \mathrm{d}\mathbf{r}, \tag{30}$$

$$E_{\text{sh},4} = +\frac{1}{4} \int \left(z_1^2 + z_2^2\right)^2 + \left(\xi^2 + \xi^2\right)^2 \mathrm{d}\mathbf{r}, \tag{31}$$

where $\xi_1 = x - \rho r_1$, $\xi_2 = y - \rho r_2$, and ϵ and k_{crit} are parameters that determine if any and what wavenumbers become critical and appear in the resulting orientation preference maps. See below for a discussion of these parameters in the case of $\alpha = 0$.

We make use of our metrics in Eq. (29). Here, the term $\delta E_{\text{sh},2}$ optimizes the neighborhood preservation. It is optimized with respect to the chosen value of α and thus the coupling between $\mathbf{z}$ and $\mathbf{x}$. In this way the term $E_{\text{sh},2}$ can be seen as analogous to the term $E_{\text{eln},2}$ in the previous model.

By applying the gradient descent, we obtain the dynamic equations

$$\partial_t \mathbf{z} = \epsilon \mathbf{z} - (\Delta + k_{\text{crit}}^2)^2 \mathbf{z} - \|\mathbf{z}\|^2 \mathbf{z} - 2\alpha k_{\text{crit}}^2 V, \tag{32}$$

$$\partial_t \xi = \epsilon \xi - (\Delta + k_{\text{crit}}^2)^2 \xi - \|\xi\|^2 \xi - 2\alpha k_{\text{crit}}^2 W, \tag{33}$$

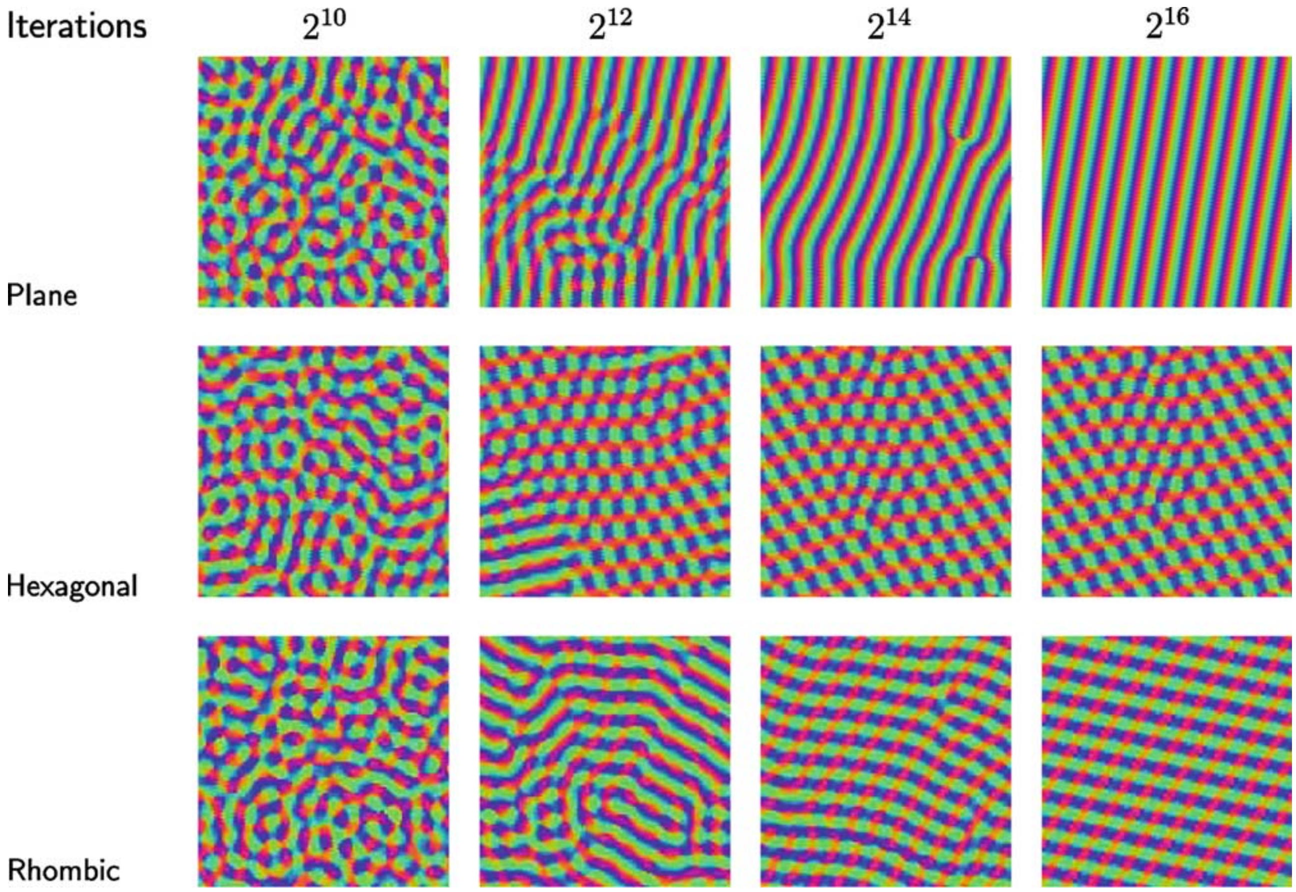

Fig. 5 Pattern formation process: Results from numerical simulations of an array of 128 × 128 neurons are depicted. The learning rate was 0.05, $\epsilon = 0.1$, and α and ρ were 0.2 and 0.15 in the plane wave, 0.35 and 0.15 in the hexagonal, and 0.23 and 0.075 in the rhombic cases. The value of the model parameter k_0 was 1.0; the scale of the simulation was set to 12 wavelengths of one side of the system

where $\xi = \xi_1 + i\xi_2$ and

$$W(\xi, \mathbf{z}) = \mathbf{z}\,\Delta\bar{\xi} + \nabla\bar{\xi}\cdot\nabla\mathbf{z} + \rho\,(1, -i)\cdot\nabla\mathbf{z}, \tag{34}$$

$$V(\xi, \mathbf{z}) = -\frac{1}{2}\,\nabla\xi\cdot\nabla\xi - \rho\,(1, i)\cdot\nabla\xi. \tag{35}$$

For $\alpha = 0$ the dynamic equations decouple and we get again

$$\partial_t\mathbf{z} = \epsilon\mathbf{z} - (\Delta + k_{\text{crit}}^2)^2\mathbf{z} - \|\mathbf{z}\|^2\mathbf{z}, \tag{36}$$

which is identical to the equation for the normal complex SH equation (as in Eq. (23)).

6 Results

We ran simulations of the Swift–Hohenberg model for a series of values of the model parameters α, ρ, k_{crit}, and ϵ in a triangular net. The maps were initialized retinotopically, i.e., $x = \rho r_1$ and $y = \rho r_2$, and with a small random orientation preference in z_1 and z_2. We investigated the progression of the map formation process with respect to the parameters used. The SH model tends to become unstable for higher learning rates due to the biharmonic operator that appears in the dynamic equations. The model was thus made stable by filtering out spatial wave numbers of less than 50%, and those of more than 150%, of k_{crit}.

The early stages of the development are similar in all cases (see Fig. 5). At later stages of the development, however, the patterns become increasingly periodic. We see different patterns evolve for different parameter sets. The final stable patterns can be distinguished by the type of the periodic patterns, which are in our case: plane wave, hexagonal and, more rare, rhomboid patterns. In the case of low values of α, plane-wave patterns typically emerge. This phenomenon has been investigated in detail by Wolf and Geisel (1998). For high values of α, we obtain periodic hexagonal patterns that contain stable pinwheels. The spectral analysis of the Swift–Hohenberg models shows a hexagonal pattern; however for some values one pair of modes seems to be weaker than the other two pairs. In extreme cases this leads to rhomboid patterns. Figure 4 shows the resulting maps, after sufficiently long

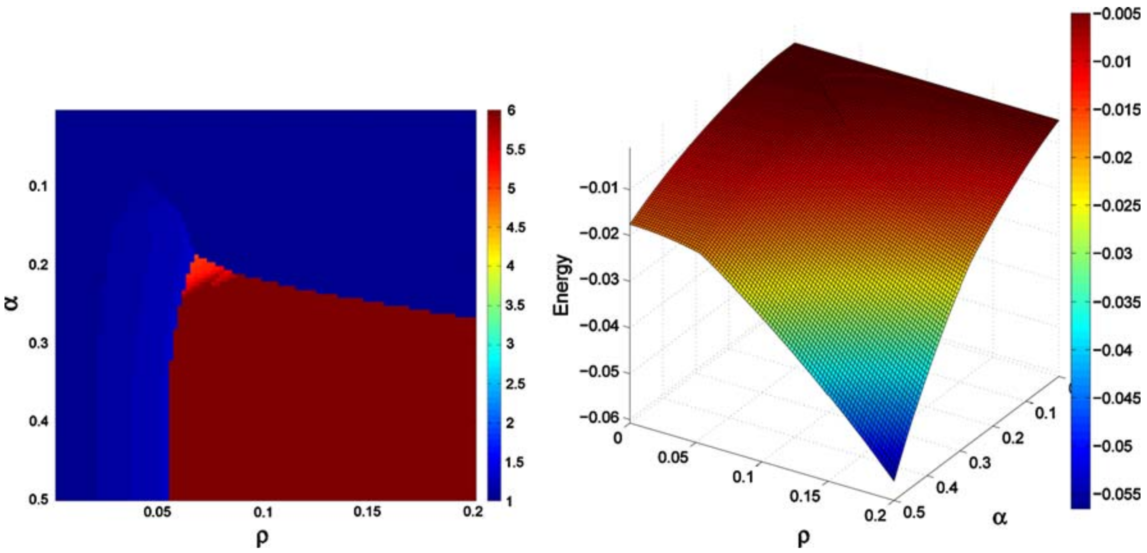

Fig. 6 Resulting stable solutions with lowest energy content (base states). *Left*: Each pixel of the graph represents a stable pattern. The color is encoded by $C = (\sum_a \|M_a\|)/\max_a(\|M_a\|)$, where high values are dark red and low values are blue. Thus, dark red pixels represent hexagonal patterns, whereas blue pixels represent the plane-wave solution. The rhombic solutions with four active modes are represented by orange to red pixels. *Right*: Energy landscape as obtained from the corresponding lowest energy states

development times, from other models of the above mentioned earlier investigations. These results are partly described in an earlier publication (Mayer et al. 2002). The number of iterations that suffices to reach the fixed point differs significantly. We used for the ELN 1.2×10^8, whereas for the SH fewer then 10^5 iterations are sufficient). The resulting pattern depends significantly on the applied metric, independent of the model used. One big difference is, however, that the SH model produces in many cases hexagonal patterns which never occurred in the previously investigated ELN models.

7 Mode analysis of the Swift–Hohenberg approach

In the following it is intended to express the dynamics of the model in terms of the modes K_a and M_a, where

$$\{\xi(\mathbf{r}), \mathbf{z}(\mathbf{r})\} = \sum_{a \in \mathcal{R}, \|a\| < 6} \{K_a, M_a\} \exp(i \mathbf{k}_a \cdot \mathbf{r}) \tag{37}$$

and $\mathbf{k}_a = k_{\text{crit}}\{\cos(a/3), \sin(a/3)\}$. Replacing ξ and $\mathbf{z}$ in the energy equation, Eq. (27), we get the energy of the modes as outlined in Appendix E. By applying gradient descent on the energy equation for the modes, the dynamics can be derived as

$$\partial_t K_a = \epsilon K_a - 2\rho\, \alpha\, k_{\text{crit}}^2\, (\mathbf{k}_a \cdot (\mathrm{i}, 1))\, M_a + \alpha N_{\mathbf{x}}^2 + N_{\mathbf{x}}^3, \tag{38}$$

$$\partial_t M_a = \epsilon M_a - 2\rho\, \alpha\, k_{\text{crit}}^2\, (\mathbf{k}_a \cdot (-\mathrm{i}, 1))\, K_a + \alpha N_{\mathbf{z}}^2 + N_{\mathbf{z}}^3, \tag{39}$$

where

$$N_{\mathbf{x}}^2 = +k_{\text{crit}}^4 \left(\bar{K}_{a+2} M_{a+1} + \bar{K}_{a+4} M_{a+5}\right), \tag{40}$$

$$N_{\mathbf{z}}^2 = +k_{\text{crit}}^4 K_{a+1} K_{a+5}, \tag{41}$$

$$N_{\mathbf{z}}^3 = -\sum_b e_{ab} \|M_b\| M_a - \sum_b f_{ab} M_b\, M_{b+3}\, \bar{M}_{a+3}, \tag{42}$$

$$N_{\mathbf{x}}^3 = -\sum_b e_{ab} \|K_b\| K_a - \sum_b f_{ab} K_b\, K_{b+3}\, \bar{K}_{a+3}, \tag{43}$$

$$e_{ab} = (2 - \delta_{ab}), \tag{44}$$

$$f_{ab} = (1 - \delta_{ab} - \delta_{a+3,b}). \tag{45}$$

8 Phase-space solutions

The local models described in Sect. 6 that are sufficiently large tend to converge to the global minimum. Thus, the analysis of the mode equations focuses on the global minima of the cost functions for each parameter setting. In Appendix D the stable and metastable states (i.e., the local minima of the cost function) of the dynamic mode equations are derived for the case $\alpha = 0$. For the other cases the analysis is more complex. Therefore, in the scope of this work a numerical analysis is preferred in order to determine the stable states. Stable states are defined as those with a global minimum value of the cost function with respect to the particular parameter settings. In the following, we discuss numerical experiments where the development under different parameter settings is tested. Since the mode dynamics tend to get stuck in a local minimum we started the simulation from three different starting conditions (a plane-wave pattern, a rhomboid pattern, a hexagonal pattern). These were the results from earlier numerical investigations and resulted in at least metastable states for certain parameter settings. Each setting was started from all four starting conditions, and the resulting patterns were then evaluated by measuring the value of the cost function. In order to visualize each result in a pixel color, the expression $C = (\sum_a \|M_a\|)/\max_a(\|M_a\|)$ was evaluated and color coded, cf. Fig. 6, where ρ (retinotopy parameter) and α (coupling strength) are varied. The other parameters are constant ($k_0 = 1$, $\epsilon = 0.1$, the learning rate was set to 0.05). The numeric integration of the time was done by Euler integration. The number of modes was six. Thus $C = 6$ represented an evenly distributed hexagonal pattern of the orientation preference. In the figure, this is represented by a dark red color. A value of $C = 1$ represents a plane-wave solution. In each pixel the states with the lowest energy are depicted. One can see, in the area between $0.06 < \rho < 0.09$ and $0.2 < \alpha < 0.25$, a kind of smooth transition from orange to brown, which represents different types of rhomboid patterns; finally the rhomboid patterns continuously transform into hexagonal patterns as the value of α and the retinotopy increases. In contrast to this we see a sharp edge from plane-wave solutions to hexagonal patterns.

In summary we see, for different values of α and ρ, plane-wave solutions, hexagonal solutions, and a wide variety of rhomboid solutions, as well as an almost continuous transition from rhomboid to hexagonal patterns.

9 Discussion

In the present work we demonstrate how the evolution of patterns can be affected by assumptions on the underlying metric of the stimulus space. We investigate this by using a modified SH model and compare the results derived from several parameters and several model types. The numerical results show that the structure is, to a high degree, dependent on the applied metrics and, to a lesser extent, on the type of the model, although differences between the investigated model types exist.

Earlier stages of the development show only small dependence on the applied metrics. At later stages of the development we found that significantly different periodic patterns emerge. In this respect the current work reproduces earlier theoretical insights (Wolf and Geisel 1998, 2003). In particular, we get, for both models, nonvanishing pinwheel densities. At later stages of development, the structure of the patterns and the pinwheel densities change in dependence on the applied metrics. From our numerical experiments with several model types this result seems to depend on the applied model to a small degree. Moreover, patterns from appropriate high-dimensional models converge to a similar structure as feature models with an overcritical value of α, i.e., a strong coupling between the features of orientation preference and position in the visual field.

Patterns of orientation preference and ocular dominance seem to be a useful field of research, providing insight into the nurture versus nature discussion. There is a view that the layout should in some way reflect the visual experience of the animal during the critical time period.[4]

Still there are open questions: for mathematical reasons the investigations consider the developmental process near the phase transition to the nonselective phase. From a biological point of view, however, there are no indications that the developmental process is subject to these conditions. Further, as in most models, it is assumed that the stimulus statistics are stationary during the developmental process. Here one may object that the retina undergoes a maturation process. A model concerning the development of receptive fields in the visual cortex shows (Mayer et al. 2001) how the shape of cortical receptive fields is affected by this process. Finally, the cortex surface is a two-dimensional manifold that is not completely flat in the sense of Gaussian curvature. Here, it also seems appropriate to extend the models to non-Euclidean geometries in the neuron space. Similar models have been suggested for technical approaches (Ritter 1999). Experiences from these models might be included in further study of the visual cortex.

The mathematical framework and the mode analysis provided may be easily merged with other approaches—in particular with the model of long-range interactions (Wolf and Geisel 2003)—and then tested against experimental maps.

Acknowledgements N.M.M. and J.M.H. thank M. Dahlem, M. Schnabel, T. Geisel, and F. Wolf for helpful hints; and K. Hosoda, S. Ikeda, and A. Hyvarinen for motivating discussions; and J. Boedecker for improving the figures. Special credit goes to David Brander for his encouraging proofreading. Last but not least N.M.M. thanks the Handai FRC of Osaka University and JST, JSPS for their financial support.

Appendix A: Gaussian distributions

With some algebraic manipulations one can calculate the distance between two Gaussian distributions (compare Eq. 1)

$$G(x, y, \mathbf{v}) = A \exp\left(-\left\|\begin{pmatrix} s_a(S) & 0 \\ 0 & s_b(S) \end{pmatrix} \cdot \hat{R}(\Phi) \cdot \begin{pmatrix} x - \langle x \rangle \\ y - \langle y \rangle \end{pmatrix}\right\|^2\right), \tag{46}$$

---

[4] For some fundamental skills it is known that they can only be achieved in a relatively brief postnatal time period known as the critical time period or critical phase. The term "critical" in this context is not directly related to any kind of dynamical criticality.

with $R(\Phi)$ being a 2×2 rotation matrix of the angle Φ. We used the constraints

$$A = 1 \tag{47}$$

$$1 = \int G^2 \mathrm{d}x\mathrm{d}y \tag{48}$$

$$\|z\| = \|\sigma_1 - \sigma_2\| \tag{49}$$

$$s_1 = 1/2\sigma_1^2 \tag{50}$$

$$s_2 = 1/2\sigma_2^2. \tag{51}$$

We then obtain the following results for the functions $a(\|z\|)$, $b(\|z\|)$, $c(\|z\|)$, and $d(\|z\|)$:

$$a(\|z\|) = \frac{\pi^2}{4}\left(\|z\|^2 + \frac{2}{\pi}\right), \tag{52}$$

$$b(\|z\|) = \frac{\pi^2}{4}\left(\frac{\|z\|^2}{4} + \frac{1}{\pi}\right), \tag{53}$$

$$c(\|z\|) = \frac{\pi^2}{2}\sqrt{\frac{\|z\|^2}{4} + \frac{1}{\pi}}, \tag{54}$$

$$h(\|z\|) = -\frac{\pi^3\|z\|^2 + 8\pi^2}{16\left(\pi\|z\|^2 + 4\right)}. \tag{55}$$

It has to be noted that the choice of the constraints in Eqs. (47–51) affect the coefficient functions $a(\|z\|)$, $b(\|z\|)$, $c(\|z\|)$, and $d(\|z\|)$. For example, all coefficients scale with the square of the amplitude A. Thus, if one chooses a different amplitude A the coefficients change accordingly.

Appendix B: General coupling terms derived from rotation symmetry

We discuss here the effect that symmetry S3 (see Sect. 3) has upon the metric tensor. After including the symmetries S1 and S2 we have a general metric tensor of the form

$$\hat{g} = \begin{pmatrix} g_{11} & g_{12} & & \\ g_{12} & g_{22} & & \\ & & g_{33} & g_{34} \\ & & g_{34} & g_{44} \end{pmatrix}. \tag{56}$$

Below we will make use of the complex form of the equation. It is equivalent to write

$$d_s^2 = \beta d\mathbf{x}\bar{d}\mathbf{x} + \gamma d\mathbf{z}\bar{d}\mathbf{z} + \nu d\mathbf{z}d\mathbf{z} + \mu d\mathbf{x}d\mathbf{x} + \text{c.c.}, \tag{57}$$

where all four scalar parameter functions β, γ, ν, and μ can be functions of $\mathbf{z}$ and $\bar{\mathbf{z}}$; the variables $\bar{d}\mathbf{z}$, $\bar{d}\mathbf{x}$, and $\bar{\mathbf{z}}$ represent the complex conjugates of $d\mathbf{z}$, $d\mathbf{x}$, and $\mathbf{z}$, respectively, and c.c. represents the complex conjugate.

The four functions β, γ, ν, and μ can obviously be expressed as functions of ϕ_z and $\|z\|$, where $\mathbf{z} = \|z\|\exp(\mathrm{i}\phi_z)$ and $\bar{\mathbf{z}} = \|z\|\exp(-\mathrm{i}\phi_z)$. The infinitesimal expressions are then accordingly

$$d\mathbf{z} = \|d\mathbf{z}\|\exp(\mathrm{i}\phi_{dz}), \tag{58}$$

$$d\mathbf{x} = \|d\mathbf{x}\|\exp(\mathrm{i}\phi_{dx}). \tag{59}$$

A combined rotation according to symmetry S3 in Sect. 3 is then

$$d\mathbf{z} = \|d\mathbf{z}\|\exp(\mathrm{i}\phi_{dz} + 2\mathrm{i}\phi), \tag{60}$$

$$d\mathbf{x} = \|d\mathbf{x}\|\exp(\mathrm{i}\phi_{dx} + \mathrm{i}\phi), \tag{61}$$

$$\mathbf{z} = \|z\|\exp(\mathrm{i}\phi_z + 2\mathrm{i}\phi), \tag{62}$$

where ϕ is used to express a rotation along the symmetry condition S3. Rotation invariance is then expressed as

$$\frac{\partial\left[d_s^2\right]}{\partial\phi} = 0, \tag{63}$$

which should be true for any ϕ in order to comply with S3. Since the symmetry should be true for all linear combinations of $\|d\mathbf{z}\|$, $\|d\mathbf{x}\|$, we get the four equations

$$\partial_\phi \beta d\mathbf{x}\bar{d}\mathbf{x} = 0, \tag{64}$$

$$\partial_\phi \gamma d\mathbf{z}\bar{d}\mathbf{z} = 0, \tag{65}$$

$$\partial_\phi \nu d\mathbf{z}d\mathbf{z} + \text{c.c.} = 0, \tag{66}$$

$$\partial_\phi \mu d\mathbf{x}d\mathbf{x} + \text{c.c.} = 0. \tag{67}$$

These equations are fulfilled if the left-hand sides of Eqs. (64–67) do not depend on ϕ. Since

$$d\mathbf{x}\bar{d}\mathbf{x} = \|dx\|^2, \tag{68}$$

$$d\mathbf{z}\bar{d}\mathbf{z} = \|dz\|^2, \tag{69}$$

$$\mathbf{z}\bar{\mathbf{z}} = \|z\|^2, \tag{70}$$

we get

$$\partial_\phi \beta = 0 \rightarrow \beta(\mathbf{z}, \bar{\mathbf{z}}) = \beta(\|z\|), \tag{71}$$

$$\partial_\phi \gamma = 0 \rightarrow \gamma(\mathbf{z}, \bar{\mathbf{z}}) = \gamma(\|z\|), \tag{72}$$

and for the remaining two terms we get

$$\partial_\phi\left[\nu(\mathbf{z}, \bar{\mathbf{z}})d\mathbf{z}d\mathbf{z} + \text{c.c.}\right] = 0 \rightarrow \partial_\phi \text{ Real}\left[\nu(\mathbf{z}, \bar{\mathbf{z}})\|dz\|^2\exp(4\mathrm{i}\phi)\right] = 0 \tag{73}$$

$$\partial_\phi\left[\mu(\mathbf{z}, \bar{\mathbf{z}})d\mathbf{x}d\mathbf{x} + \text{c.c.}\right] = 0 \rightarrow \partial_\phi \text{ Real}\left[\mu(\mathbf{z}, \bar{\mathbf{z}})\|dx\|^2\exp(2\mathrm{i}\phi)\right] = 0. \tag{74}$$

Since the last equations have to be true for any ϕ even

$$\partial_\phi\left[\nu(\mathbf{z}, \bar{\mathbf{z}})\|dz\|^2\exp(4\mathrm{i}\phi)\right] = 0 \tag{75}$$

$$\partial_\phi\left[\mu(\mathbf{z}, \bar{\mathbf{z}})\|dx\|^2\exp(2\mathrm{i}\phi)\right] = 0 \tag{76}$$

is necessary in order to fulfil the symmetry S3. From these equations we can obviously deduce the following constant expressions:

$$\left[\nu(\mathbf{z},\bar{\mathbf{z}})\|dz\|^2\exp(4\mathrm{i}\phi)\right] = \text{const.} \tag{77}$$

$$\left[\mu(\mathbf{z},\bar{\mathbf{z}})\|dx\|^2\exp(2\mathrm{i}\phi)\right] = \text{const.} \tag{78}$$

Since in both equations the terms $\exp(4\mathrm{i}\phi)$ and $\exp(2\mathrm{i}\phi)$ show a covariant behavior to ϕ, the corresponding multiplicand must be contravariant. The only possible argument to contravariant expressions is $\bar{\mathbf{z}} = \|z\|\exp(-2\mathrm{i}\phi)$. Thus, the shape of ν and μ must be

$$\nu(\mathbf{z},\bar{\mathbf{z}}) = \mathbf{h}(\|z\|)\bar{\mathbf{z}}^2, \tag{79}$$

$$\mu(\mathbf{z},\bar{\mathbf{z}}) = \mathbf{c}(\|z\|)\bar{\mathbf{z}}. \tag{80}$$

We cannot exclude beforehand that we have to assume $\mathbf{h}(\|z\|)$ and $\mathbf{c}(\|z\|)$ to be complex, i.e., there are actually four real-valued functions

$$\mathbf{h}(\|z\|) = h_r(\|z\|) + \mathrm{i}h_i(\|z\|), \tag{81}$$

$$\mathbf{c}(\|z\|) = c_r(\|z\|) + \mathrm{i}c_i(\|z\|). \tag{82}$$

Considering $d_s^2 = \text{Real}(\ldots)$ as a metric, one can use the relation

$$\begin{aligned} &d_s^2(z_1, z_2, dz_1, dz_2 = 0, dx = 0, dy = 0) \\ &\quad = d_s^2(z_1, z_2, -dz_1, dz_2 = 0, dx = 0, dy = 0). \end{aligned} \tag{83}$$

From this equation one can get, after some straightforward calculations, $h_i = 0$; h is a real value and we get in terms of real variables

$$C_{zz} = h(\|z\|)\left(\begin{pmatrix} z_1 \\ z_2 \end{pmatrix}^T \begin{pmatrix} dz_1 \\ dz_2 \end{pmatrix}\right)^2. \tag{84}$$

Finally $\mathbf{c}(\|\mathbf{z}\|)$ can be expressed as $\mathbf{c} = c(\|z\|)\exp(\mathrm{i}\psi(\|z\|))$. Then the corresponding coupling term C_{cx} becomes

$$C_{xz} = c(\|z\|)\begin{pmatrix} z_1 \\ z_2 \end{pmatrix}^T \mathbf{T}(\psi(\|z\|))\begin{pmatrix} dx^2 - dy^2 \\ 2dxdy \end{pmatrix}. \tag{85}$$

Note that, at this point, ψ can be a function of $\|z\|$. However, the following part shows that $\psi(\|z\|) = \text{const}$. This can be seen from the following steps. We use the reflection symmetries S2. Consider the case when

$$\begin{pmatrix} z_1 \\ z_2 \end{pmatrix}^T \mathbf{T}(\psi(\|z\|)) = \begin{pmatrix} 1 \\ 0 \end{pmatrix}. \tag{86}$$

In this case C_{xz} has the form

$$C_{xz} = c(\|z\|)\begin{pmatrix} 1 \\ 0 \end{pmatrix}^T \begin{pmatrix} dx^2 - dy^2 \\ 2dxdy \end{pmatrix}. \tag{87}$$

Obviously, this term is reflection symmetric to inverting $(dx, dy) = (1, 0)$ and $(dx, dy) = (0, 1)$. It is not symmetric to inversions in any other direction. For other values of ψ another pair of orthogonal symmetry axes appear. Thus, the parameter ψ indicates the projections of the symmetry axes in spatial space. Since these symmetry axes merely depend on the orientation ($\arctan(\mathbf{z})$)—and not on the orientation strength $\|z\|$—it follows that $\psi(\|z\|)$ is constant. Thus, under the symmetry constraints S1–S3 we get

$$C_{xz} = c(\|z\|)\begin{pmatrix} z_1 \\ z_2 \end{pmatrix}^T \mathbf{T}(\psi)\begin{pmatrix} dx^2 - dy^2 \\ 2dxdy \end{pmatrix}. \tag{88}$$

It should be noted that these transformations affect integrals over the stimulus space. These integrals appear in the ELN approach and, implicitly, due to the appearance of a random stimulus, also in Kohonen's SOM (in the sense of a Monte Carlo approach). Thus, in contrast to the SH model, the maps are affected by such transformations.

Appendix C: Regauging the feature metric

The metrics Eq. (11) can be further simplified by rescaling or regauging the coordinates in the feature space. Of course not every redefinition is appropriate. In the following we only discuss redefinitions that

- comply with the symmetries S1–S3,
- do not change the appearance of the orientation maps, and
- do not affect the dynamics of the Swift–Hohenberg model in any way except for rescaling the solutions.

We start with a simpler special discussion that is in fact restricted to linear rescaling of the feature space. The methods can be applied relatively easily analytically. The disadvantage is that it is only valid near $\|z\| \approx 0$.

In the second part of this appendix we discuss the more general case of any $\|z\|$.

C.1 Part 1: $\|z\| \approx 0$

For this part we concentrate on small values of $\|z\|^2$. In this case the metric can be approximated by

$$\begin{aligned} d_s^2 &= a(z=0)d\mathbf{x}d\bar{\mathbf{x}} + c(z=0)\bar{\mathbf{z}}d\mathbf{x}^2 \\ &\quad + b(z=0)d\mathbf{z}d\bar{\mathbf{z}} + O(\|z\|^2). \end{aligned} \tag{89}$$

Since the part of d_s^2 related to h is of order $\|z\|^2$, it diminishes faster than the other terms of the equation and shall be neglected.

We can redefine

$$dx_{\text{new}} = \sqrt{a(0)}dx_{\text{old}}, \tag{90}$$

$$dy_{\text{new}} = \sqrt{a(0)}dy_{\text{old}}, \tag{91}$$

$$z_{1,\text{new}} = \sqrt{b(0)}z_{1,\text{old}}, \tag{92}$$

$$z_{2,\text{new}} = \sqrt{b(0)}z_{2,\text{old}}. \tag{93}$$

Then the distance measure becomes

$$d_s^2 = \mathrm{Re}\left(d\mathbf{x}d\bar{\mathbf{x}} + \alpha\bar{\mathbf{z}}d\mathbf{x}^2 + d\mathbf{z}d\bar{\mathbf{z}}\right), \tag{94}$$

where α is

$$\alpha = \frac{c_{\mathrm{old}}(0)}{a_{\mathrm{old}}(0)\sqrt{b_{\mathrm{old}}(0)}}. \tag{95}$$

The metric tensor then becomes

$$\hat{g}_\alpha = \begin{pmatrix} 1+\alpha z_1 & \alpha z_2 & & \\ \alpha z_2 & 1-\alpha z_1 & & \\ & & 1 & \\ & & & 1 \end{pmatrix}, \tag{96}$$

by redefining the orientation strength ($\|z\|^2$).

C.2 Part 2: $\|z\| \gg 0$

For finite $|z|$ one can consider to map the metric to simpler metric by redefining $|z|$. This is then useful if the dynamics of the model only depends on the metric and not explicitly on $|z|$. So, investigating the equivalence class would be sufficient to investigate the corresponding metrics of the same equivalence class, which has the property $h = 0$. In this way the search space can be reduced significantly.

In the following a way is shown to reduce an arbitrary metric to an equivalence class where the coupling term C_{zz} vanishes, i.e., the function $h(\|z\|)$ becomes 0.

This is possible if we redefine the orientation strength $\zeta = \|z_{\mathrm{old}}\|^2$ as $z_{\mathrm{new}} = \tilde{f}(\zeta)z_{\mathrm{old}}$. Thus, we have

$$z_{1,\mathrm{new}} = z_{1,\mathrm{old}}\tilde{f}(\zeta), \tag{97}$$

$$z_{2,\mathrm{new}} = z_{2,\mathrm{old}}\tilde{f}(\zeta). \tag{98}$$

In addition, a constant rescaling of the retinal coordinates is also possible, as we used in the previous example. Thus, we have

$$x_{\mathrm{new}} = x_{\mathrm{old}}/C_1 \tag{99}$$

$$y_{\mathrm{new}} = y_{\mathrm{old}}/C_1, \tag{100}$$

after rescaling. This means that the direction of the preferred orientation remains the same. The aim is now to derive a metric tensor of the form:

$$\hat{g}_{\mathrm{new}} = \begin{pmatrix} a_{\mathrm{new}} + c_{\mathrm{new}}z_{1,\mathrm{new}} & c_{\mathrm{new}}z_{2,\mathrm{new}} & & \\ c_{\mathrm{new}}z_{2,\mathrm{new}} & a_{\mathrm{new}} - c_{\mathrm{new}}z_{1,\mathrm{new}} & & \\ & & b_{\mathrm{new}} & \\ & & & b_{\mathrm{new}} \end{pmatrix}. \tag{101}$$

We use the ansatz

$$\begin{aligned} b_{\mathrm{new}}(dz_{1,\mathrm{new}}^2 + dz_{2,\mathrm{new}}^2) = b_{\mathrm{old}}&(dz_{1,\mathrm{old}}^2 + dz_{2,\mathrm{old}}^2) \\ &+ h_{\mathrm{old}}(dz_{1,\mathrm{old}}z_{1,\mathrm{old}} \\ &+ dz_{2,\mathrm{old}}z_{2,\mathrm{old}}). \end{aligned} \tag{102}$$

By comparing the coefficients $dz_{1,\mathrm{old}}^2 + dz_{2,\mathrm{old}}^2$ and $dz_{1,\mathrm{old}}z_{1,\mathrm{old}} + dz_{2,\mathrm{old}}z_{2,\mathrm{old}}$, we obtain

$$b_{\mathrm{old}} = b_{\mathrm{new}}\tilde{f}^2, \tag{103}$$

$$h_{\mathrm{old}} = 4b_{\mathrm{new}}(\tilde{f}\tilde{f}' + \zeta\,\tilde{f}'^2). \tag{104}$$

Taking the quotient $r(\zeta) = h_{\mathrm{old}}/b_{\mathrm{old}}$, we obtain a quadratic equation

$$\zeta\,F^2(\zeta) + F(\zeta) - r(\zeta) = 0, \tag{105}$$

where $F = \tilde{f}'/\tilde{f}$. The most convenient form of the solutions to Eq. (105) is $F_{1,2} = 2r/(1 \pm \sqrt{1 + 4\,\zeta\,r})$, of which only

$$F(\zeta) = 2\,r(\zeta)/\left(1 + \sqrt{1 + 4\,\zeta\,r(\zeta)}\right) \tag{106}$$

is continuous at $\zeta = 0$. Since $\int F = \log(\tilde{f})$ we get

$$\tilde{f}(\zeta) = f(\zeta)/C_2 = \exp\left(\int_0^\zeta F(\xi)\,\mathrm{d}\xi\right)/C_2, \tag{107}$$

where C_2 is a free constant that originates from the integration, and

$$f(\zeta) = \exp\left(\int_0^\zeta 2\,r(\xi)/\left(1 + \sqrt{1 + 4\,\xi\,r(\xi)}\right)\right) \tag{108}$$

is introduced for the sake of convenience ($f(0) = 1$). The coefficients a_{new}, b_{new}, and c_{new} become

$$a_{\mathrm{new}}(\zeta) = C_1^2 a_{\mathrm{old}}, \tag{109}$$

$$b_{\mathrm{new}}(\zeta) = C_2^2 b_{\mathrm{old}}/f^2, \tag{110}$$

$$c_{\mathrm{new}}(\zeta) = C_2 C_1^2 c_{\mathrm{old}}/f. \tag{111}$$

Please note that a_{new}, b_{new}, and c_{new} are expressions of ζ, that is, $\|z_{\mathrm{old}}\|^2$, and have to be transformed into expressions[5] of $\|z_{\mathrm{new}}\|^2$.

The resulting metric under the new coordinates is then

$$d_s^2 = \mathrm{Real}\left(a_{\mathrm{new}}d\mathbf{x}d\bar{\mathbf{x}} + b_{\mathrm{new}}d\mathbf{z}d\bar{\mathbf{z}} + c_{\mathrm{new}}\bar{\mathbf{z}}d\mathbf{x}^2\right). \tag{112}$$

Please note that this metric is an exact transformation.

Finally in order to come back to the first considerations, the general metric can be considered for a very weak orientation strength ($\zeta \approx 0$). By choosing

$$C_1^2 = 1/a_{\mathrm{old}}(0) \tag{113}$$

$$C_2^2 = 1/b_{\mathrm{old}}(0) \tag{114}$$

---

[5] It should be noted that analogous considerations do not result in the elimination of a, or b or c but would result in $\tilde{f} = 0$.

we get

$$\hat{g}_{\text{new},\zeta\approx 0} = \hat{g}_{\alpha} = \begin{pmatrix} 1+\alpha\, z_{1,\text{new}} & \alpha\, z_{2,\text{new}} & & \\ \alpha\, z_{2,\text{new}} & 1-\alpha\, z_{1,\text{new}} & & \\ & & 1 & \\ & & & 1 \end{pmatrix} + \mathbf{O}(\zeta), \tag{115}$$

where $\alpha = \text{const.} = c_{\text{new}}(0)$, which gives the same equation for α as in the previous discussion for $\|z\| \approx 0$. Straightforward calculations then give the same value for α as in Eq. (95).

Appendix D: Stability analysis of three types of regular patterns

Here we investigate marginally stable states (i.e., local minima) of our model, for the plane case ($\alpha = 0$), and show that both a rhomboid state and a plane-wave state are marginally stable at the same time in this case. In this case ($\alpha = 0$) our model is identical to previously investigated models: one of two possible stable configurations that have been overlooked in previous works (Wolf and Geisel 1998), which are two types of the rhomboid case. The plane cases are:

- Nonselective case
- Plane-wave solutions
- Rhomboid patterns

The dynamic equations are (cf. Eq. (39))

$$\begin{aligned} &\partial_t M_{a/N} \\ &\quad = \epsilon M_{a/N} - \sum_b e_{ab} \|M_b\| M_a - \sum_b f_{ab} M_b\ M_{b+3}\ \bar{M}_{a+3}, \end{aligned} \tag{116}$$

where

$$e_{ab} = (2 - \delta_{ab}) \tag{117}$$

$$f_{ab} = (1 - \delta_{ab} - \delta_{a+3,b}). \tag{118}$$

Moreover the energy equation of the plane case is (cf. Appendix E)

$$\begin{aligned} U = &-\frac{\epsilon}{2} \sum_a \|{M_a}^2\| + \frac{1}{4} \sum_{a,b} e_{ab} \|{M_a}^2\| \|{M_b}^2\| \\ &+ \frac{1}{4} \sum_{a,b} f_{ab} M_a M_{a+3}\ \bar{M}_b \bar{M}_{b+3}. \end{aligned} \tag{119}$$

The gradient of the cost function results in the learning rule in Eq. (116). The local minima are fixed points of the dynamics. For the stability analysis it is useful to separate the complex variable

$$M_a = \mathcal{M}_a \times \exp(\mathrm{i}\phi_a) \tag{120}$$

into the positive-definite real-valued amplitude $\mathcal{M}_a$ and the phase ϕ_a. The equation of energy Eq. (119) becomes

$$\begin{aligned} U = &-\frac{\epsilon}{2} \sum_a \mathcal{M}_a^2 + \frac{1}{4} \sum_{a,b} e_{ab} \mathcal{M}_a^2 \mathcal{M}_b^2 \\ &+ \frac{1}{4} \sum_{a,b} f_{ab} \times Q_{ab} \times \cos(\Phi_{ab}), \end{aligned} \tag{121}$$

where

$$Q_{ab} = \mathcal{M}_a \mathcal{M}_{a+3}\ \mathcal{M}_b \mathcal{M}_{b+3}, \tag{122}$$

$$\Phi_{ab} = (\phi_a - \phi_{a+3}) + (\phi_b - \phi_{b+3}). \tag{123}$$

Gradient descent gives for $\mathcal{M}_a$ and ϕ_a

$$\begin{aligned} \partial \mathcal{M}_a = &\ \epsilon \mathcal{M}_a - \sum_b e_{ab}\ \mathcal{M}_b^2 \mathcal{M}_b \\ &- \sum_b f_{ab}\ \mathcal{M}_b \mathcal{M}_{b+3} \mathcal{M}_{a+3} \cos(\Phi_{ab}), \end{aligned} \tag{124}$$

$$\partial \phi_a = \sum_b f_{ab}\ \mathcal{M}_b \mathcal{M}_{b+3} \mathcal{M}_a \mathcal{M}_{a+3} \sin(\Phi_{ab}). \tag{125}$$

Stationary points are all the points that fulfill

$$\partial \mathcal{M}_a = 0, \tag{126}$$

$$\partial \phi_a = 0. \tag{127}$$

In the following we name examples and check the eigenvalues of the Jacobian matrix. In this way we can find out whether these points are indeed marginally stable.

D.1 Plane waves

We assume that all modes are equal to zero except for mode $\mathcal{M}_0$. Since the mode $\mathcal{M}_3$ is nonexistent (=0), the right-hand side of Eq. (125) vanishes, as does the second term of the amplitude equations, and the amplitude equations become

$$\partial \mathcal{M}_0 = \epsilon \mathcal{M}_0 - \mathcal{M}_0^3. \tag{128}$$

The equilibrium point is $\mathcal{M}_0 = \sqrt{\epsilon}$. Its stability can be accessed easily from the derivative of the equation around this stationary point—the Jacobian is one dimensional in this case.

D.2 Rhomboid case

We assume two active mode pairs—a total of four modes—that all have the same amplitude $\mathcal{M}_0$. Since this is different from the single-mode case, Eq. (125) does not vanish and we set $\Phi_{jn} = \pm\pi$; thus the amplitude equations become

$$\begin{aligned} \partial_t \mathcal{M}_a &= \epsilon \mathcal{M}_a - \sum_b e_{ab}\ \mathcal{M}_b^2 \mathcal{M}_a \\ &= \sum_b f_{ab}\ \mathcal{M}_b \mathcal{M}_{b+3} \mathcal{M}_{a+3}. \end{aligned} \tag{129}$$

We assume the same amplitude for all modes and get for the equilibrium point

$$0 = \epsilon \mathcal{M}_0 - \left(\sum_b e_{ab}\right)\mathcal{M}_0^3 + \left(\sum_b f_{ab}\right)\mathcal{M}_0^3. \qquad (130)$$

Since $\sum_b e_{ab} = 7$ and $\sum_n f_{ab} = 2$, we get

$$\mathcal{M}_0 = \sqrt{\epsilon / \left(\left(\sum_b e_{ab}\right) - \left(\sum_b f_{ab}\right)\right)} = \sqrt{\frac{\epsilon}{5}}. \qquad (131)$$

The stability of the equilibrium state can be seen from the Jacobian matrix for $m_a = M_a - M_0$. We get:

$$\begin{aligned}\partial m_a &= \epsilon\ m_a - \mathcal{M}_0^2 \sum_n (e_{ab}(2m_b + m_a)) \\ &\quad + \mathcal{M}_0^2 \sum_c (f_{ab}(m_b + m_{b+3} + m_{a+3})). \qquad (132)\end{aligned}$$

We remember that $\epsilon = 5\mathcal{M}_0^2$ and we finally obtain

$$\begin{aligned}\partial_t m_a &= \mathcal{M}_0^2 \left(\left(\sum_b e_{ab}\right) - \left(\sum_b f_{ab}\right)\right) m_a \\ &\quad - \mathcal{M}_0^2 \sum_b e_{ab}(2m_b + m_a) \\ &\quad + \mathcal{M}_0^2 \sum_b f_{ab}(m_b + m_{b+3} + m_{a+3}). \qquad (133)\end{aligned}$$

Thus

$$\begin{aligned}\partial_t m_a &= \mathcal{M}_0^2 \left(-2 \sum_b e_{ab} m_b \right. \\ &\quad \left. + \sum_n e_{ab}(m_b + m_{b+3} + m_{a+3} - m_a) \right). \qquad (134)\end{aligned}$$

Rearranging and sorting according to the coefficients m_b and $m_a = \sum_b m_b \delta_{ab}$ we get

$$\partial_t m_a = \sum_b J_{ab} m_b, \qquad (135)$$

where the Jacobian reads

$$J_{ab} = -2e_{ab} + f_{ab} + f_{a,b+3} + (\delta_{a,b+3} - \delta_{a,b}) \sum_c f_{ac}. \qquad (136)$$

Since

$$e_{ab} = 2 - \delta_{ab}, \qquad (137)$$

$$f_{ab} = 1 - \delta_{ab} - \delta_{a,b+3}, \qquad (138)$$

we get finally

$$J_{ab} = -2 - 2\delta_{ab}, \qquad (139)$$

which is a negative-definite matrix. Hence rhomboid patterns are stable.

D.3 Three modes and three antimodes

Finally, it is possible to discuss the stability of three modes and the corresponding antimodes. Since in the case $\alpha = 0$ no relations between the $\mathbf{k}_a$ appear in the equations, the arrangement of the active modes is arbitrary and not necessarily hexagonal. For the equilibrium, we get

$$\Phi_{ab} = \pm\frac{3\pi}{2}; \quad \mathcal{M}_0 = \sqrt{\frac{\epsilon}{3}}. \qquad (140)$$

Further analysis shows that this state is stable. However, one eigenvalue of the Jacobian is zero.

Appendix E: Energy in terms of modes

Mode equations (Eqs. 38 and 39) can be expressed as the gradient of a cost function

$$\begin{aligned}U_x &= -\frac{\epsilon}{2}\sum_a \|K_a\|^2 + \frac{1}{4}\sum_{a,b} e_{ab}\|K_a\|^2\|K_b\|^2 \\ &\quad + \frac{1}{4}\sum_{a,b} f_{ab} K_a K_{a+3} \bar{K}_b \bar{K}_{b+3}, \qquad (141)\\ U_z &= -\frac{\epsilon}{2}\sum_a \|M_a\|^2 + \frac{1}{4}\sum_{a,b} e_{ab}\|M_a\|^2\|M_b\|^2 \\ &\quad + \frac{1}{4}\sum_{a,b} f_{ab} M_a M_{a+3} \bar{M}_b \bar{M}_{b+3}, \qquad (142)\\ U_{xz} &= -\frac{k_{\text{crit}}^4}{2}\left(\sum_a K_a \bar{M}_{a+1} K_{a+2} + \bar{K}_a M_{a+1} \bar{K}_{a+2}\right), \qquad (143)\\ U_{\text{ret}} &= -\rho k_{\text{crit}}^2 \left(\sum_a (\mathrm{i}, -1)\cdot k_a K_a \bar{M}_a\right) + \text{c.c.}, \qquad (144)\\ U &= U_x + U_z + \alpha(U_{xz} + U_{\text{ret}}). \qquad (145)\end{aligned}$$

References

Cross MC, Hohenberg PC (1993) Pattern formation outside equilibrium. Rev Mod Phys 65(3):851–1112

Durbin R, Willshaw D (1987) An analogue approach to the traveling salesman problem using an elsatic net algorithm. Nature 326:689–691

Ernst U, Pawelzik K, Sahar-Pikielny C, Tsodyks M (2001) Intracortical origin of visual maps. Nat Neurosci 4:431–436

Freeman RD, et al (1997) Clustering of response properties of neurons in the visual cortex. In: Social Neuroscience, 23:227.1

Jones J, Palmer L (1987) The two-dimensional spatial structure of simple receptive fields in cat striate cortex. J Neurophys 58:1187–1211

Kaschube M, Wolf F, Geisel T, Loewel S (2001) The prevalance of colinear contours in the real world. Neurocomputing 38(40):1335–1339

Kohonen T (2001) Self-organizing maps. Springer, Heidelberg

Liu Z, Gaska JP, Jacobson LD, Pollen DA (1991) Interneural interaction between members od quadrature pairs in the cat's visual cortex. Vision Res 32:1193–1198

Löwel S (1998) The layout of orientation and ocular dominance domains in area 17 of strabismic cats. Eur J Neurosci 10(8):2629–43

Mayer NM, Herrmann MJ, Theo Geisel (1998) A cortical interpretation of ASSOMs. In: Proceedings of International Conference on Artificial Neural Networks (ICANN), vol 2, pp 961–966

Mayer NM, Herrmann JM, Geisel T (2002) Curved feature metrices in models of visual cortex. Neurocomputing 44–46(C):533–539

Mayer NM, Herrmann JM, Geisel T (2003) Shaping of receptive fields in visual cortex during retinal maturation. J Comp Neurosci 15(3):307–320

Pollen D, Ronner S (1981) Phase relationships betweeen adjacent simple cells in the visual cortex. Science 212:1409–1411

Riesenhuber M, Bauer H-U, Brockmann D, Geisel T (1998) Breaking rotational symmetry in a self-organizing map model for orientation map development. Neural Comput 10:717–730

Ritter H (1999) Self-organizing maps in non-Euclidean spaces. In: Oja E, Kaski S (eds) Kohonen Maps, pp 97–108

Ritter H, Martinetz T, Schulten K (1992) Neuronale netze. Addison Wesley, Bonn

Sengpiel F, Bonhoeffer T, Stawinski P (1999) Influence of experience on orientation maps in cat visual cortex. Nat Neurosci 2:727–732

Swindale NV (1996) The development of topography in the visual cortex: a review of models. Network 7:161–247

Swindale NV, Shoham D, Grinvald A, Bonhoeffer T, Hübener M (2000) Optimizing coverage in the cortex. Nat Neurosci 3(8):750–751

Thomas PJ, Cowan JD (2003) Symmetry induced coupling of cortical feature maps. Phys Rev Lett 92(18810)

Malsburg Cvd (1973) Self-organization of orientation sensitive cells in striate cortex. Kybernetik 14:49–54

Wolf F (2005) Symmetry, multistability, and long-range interactions in brain development. Phys Rev Lett 95(208701)

Wolf F, Geisel T (1998) Spontaneous pinwheel annihilation during visual development. Nature 395:73–78

Wolf F, Geisel T (2003) Universality in visual cortical pattern formation. J Phys 97:253–264